Electronic properties of solution-processed Cu(In,Ga)(S,Se)$_2$ solar cells using metal chalcogenides and amine-thiol solvent mixtures

Soňa Uličná[1], Mustafa Togay[1], Martin Bliss[1], Vincent Tsai[1], Lewis D. Wright[1], Jamie Lowe[1,2], Andrei V. Malkov[2], John M. Walls[1] and Jake W. Bowers[1]

[1]CREST, Wolfson School of Mechanical, Electrical and Manufacturing Engineering, [2]Department of Chemistry, School of Science, Loughborough University, Loughborough, Leicestershire, LE11 3TU, UK

Abstract — This work examines the effects of post-deposition air-annealing on the electronic properties of solution-processed heterojunction CIGS solar cells. The annealing in air of the CIGS/CdS interface was found to have positive effects on the device performance with an increase in all PV parameters even after annealing times as short as 5 min. A V_{OC} increase of < 130 mV was caused by the reduced surface and grain boundary recombination through passivation of surface Se deficiencies with oxygen atoms. Prolonged annealing causes charge redistribution and diffusion of mobile elements such as Cu and Cd deeper into the absorber bulk however, resulting in lower carrier density and deeper defects with increased annealing time. These were observed through capacitance-voltage profiling and admittance spectroscopy.

Index Terms — air-annealing, amine-thiol solvent combination, CIGS, solar cells, solution-processing.

I. INTRODUCTION

Cu(In,Ga)(S,Se)$_2$ solar cells are an efficient thin-film photovoltaic technology which provides an opportunity for a considerable capital cost reduction when fabricated using atmospheric processes. Atmospheric deposition utilizing molecular solutions and simple, cost-effective and large-area compatible deposition methods such as spraying is a promising route for CIGS solar cells. Other advantages interesting for industrial application include high material utilization, composition uniformity, production yield and throughput.

Currently, the highest performing solution-based approach yielded 15.2% power conversion efficiency (PCE) [1]. This method used the highly toxic and explosive solvent hydrazine to dissolve metal chalcogenides. Metal chalcogenides as a precursor material are preferable due to their impurity free character, however they are insoluble in most of the common benign solvents. Consequently, our group has focused on using a safer amine-thiol solvent mixture to dissolve metal chalcogenides, retaining the excellent precursor material whilst removing the hazardous aspect of the hydrazine method. In this technique, metal chalcogenides including copper and indium sulfides and gallium with selenium are easily dissolved in a combination of 1,2-ethaneditihol/1,2-ethylenediamine. The final precursor solution with optimized and tunable [Cu]/[Ga+In] and [Ga]/[Ga+In] ratios, after being sprayed onto Mo-coated glass and annealed in selenium atmosphere, resulted in CIGS solar cells exceeding 9% efficiency [2]. The purpose of this work is to analyze the effect of post-deposition air-annealing treatment to improve the electrical quality of the solution-processed CIGS solar cells. The air-annealing step has been found important to achieve high performance CIGS devices by modifying the CIGS heterojunction interface properties, suppressing surface recombination and hence increasing open circuit voltages (V_{OC}) [3]. Excessive annealing can cause Cu and Cd atom migration however. These then act as compensating donors, reducing the carrier concentration of the CIGS [4]. The annealing duration therefore has to be carefully controlled. Air-annealing of the CIGS/CdS films in air was performed for durations from 0 to 60 min. In our previous work we focused on optimization of the deposition and post-deposition processes. Here we concentrate on the analysis of electrical behavior and defect distribution of the solution-processed CIGS absorber material prepared from metal chalcogenides in amine/thiol solvent mixture. A deeper understanding of electronic properties is essential to identify limiting factors of the device performance, however interpretation of profiles such as admittance spectra or capacitance-voltage charge carrier profiles are very difficult and controversial, relying on many assumptions [5].

II. EXPERIMENTAL DETAILS

The CIGS precursor solution was prepared by dissolving copper sulfide (Cu$_2$S), indium sulfide (In$_2$S$_3$) and gallium with selenium separately in a mixture of 1,2-ethanedithiol/1,2-ethylenediamine 1/10 (v/v) ratio. The individual solutions were then mixed together to form a final precursor solution with intended Cu$_{0.9}$In$_{0.7}$Ga$_{0.3}$(S,Se)$_2$ composition. This was then deposited by spraying onto a Mo/MoN$_x$/Mo coated glass substrate. The detailed procedure of the solution preparation and deposition is described in our previous work [6]. The MoN$_x$ serves as a barrier layer against excessive MoSe$_2$ formation [7]. The as-deposited absorber was contained in a graphite box together with selenium pellets, placed inside a tube furnace and heated at 540°C for 90 min (including ramping). The tube was filled with nitrogen and the starting pressure was set to 450 Torr prior the start of the selenization. Applying the MoN$_x$ barrier, only a thin MoSe$_2$ layer forms at the Mo/CIGS interface. This allows for longer selenization

dwells, resulting in higher absorber crystallinity without compromising the film adhesion [6]. The CdS buffer layer of approximately 50 nm was deposited by chemical bath deposition (CBD) using $CdSO_4$ and thiourea as Cd and S precursors respectively and NH_4OH as a complexing agent. A furnace air-annealing of the CIGS/CdS films was performed at 180°C in ambient conditions for various durations. The CIGS solar cells were completed by RF sputtering of iZnO and Al-doped ZnO and evaporation of an Ag grid. The individual samples were delimited into cells of 0.25 cm^2 total area by mechanical scribing.

Current density-voltage (J-V) characteristics were measured using an ABET solar simulator under 1000 W/m^2 illumination calibrated using a reference Si cell. The external quantum efficiency (EQE) spectra were acquired using a Bentham PVE300 system at 0 V bias with a spectral resolution of 5 nm. The electroluminescence (EL) images were obtained using an Apogee Alta F800 camera, with a Quioptiq Inspec X IR lens with an aperture f-stop of 2.8. Each cell was placed in forward bias, with a current injection of ~J_{SC} and images were collected using 10 min acquisition time. Temperature-dependent electrical measurements such as admittance spectroscopy (AS) and J-V-T were conducted using an evacuated closed-cycle helium cryostat. The temperature is controlled in a range 105 – 315 K using a LakeShore 335 temperature controller. Prior to the measurements, the samples were kept in dark for 1 h to ensure a relaxed state. Admittance spectroscopy data was acquired using Keysight E4990A impedance analyzer operating at frequencies from 100 Hz to 1 MHz at zero bias conditions. Capacitance-voltage (C-V) measurements were performed using the same impedance analyzer. The voltage was swept from -1 V to 1 V at a frequency of 100 kHz at room temperature. J-V-T was performed using a Keysight B2902A measurement unit and a halogen light source. Spectrally-resolved photoluminescence (PL) was conducted using a home-made measurement system. The excitation source used was a pulsed picosecond laser with a wavelength of 640 nm and the sample was excited at a laser pulsed rate of 40 MHz.

III. RESULTS

After the CBD CdS treatment, four identical CIGS/CdS films were annealed in a furnace preheated to 180°C for 5, 15, 30 and 60 min in air. A non-annealed sample was used as a reference. PV performance parameters including open circuit voltage (V_{OC}), short circuit current density (J_{SC}), fill factor (FF) and power conversion efficiency (PCE) extracted from the J-V measurements of approximately 15 cells for each annealing duration are summarized in box plots in Fig. 1. All performance indicators increased with annealing time up to 30 min. Annealing for 60 min resulted in very scattered PCEs with no additional improvement from the 30 min annealing. On the contrary a decrease in fill factor is observed and

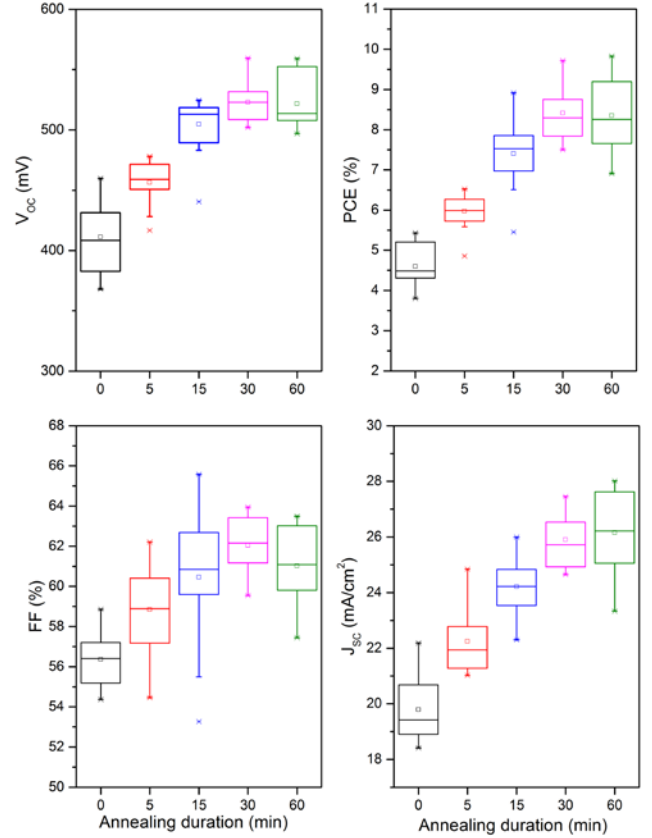indicates the beginning of degradation of the device performance.

Fig. 1. PV parameters for various CIGS/CdS air-annealing durations.

Fig. 2 compares J-V curves of the champion cells for each annealing duration. All key performance indicators corresponding to the curves in Fig. 2 are summarized in Table I. It is observed that air-annealing for as short as 5 min starts to improve all device parameters and after 15 min a significant improvement in the device performance can be seen with PCE escalating from an initial 5.4% to above 9%. This remarkable improvement in device performance originates mainly from a significant increase in V_{OC} by over 130 mV from 0 to 30 min of air-annealing. Improvements in J_{SC} and FF are also non-negligible.

TABLE I
PV PARAMETERS OF THE CHAMPION CELL FOR EACH AIR-ANNEALING DURATION

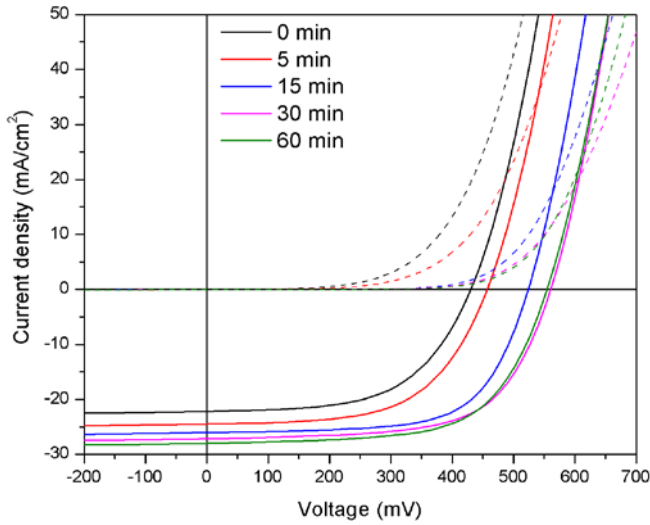|	V_{OC} (mV)	J_{SC} (mA/cm^2)	FF (%)	PCE (%)
0 min	429.0	22.2	57.1	5.4
5 min	455.8	24.4	58.6	6.5
15 min	523.1	26.0	65.6	8.9
30 min	559.4	27.2	63.9	9.7
60 min	553.5	28.0	63.5	9.8

Fig.2. Light and dark J-V curves of the champion cell for each air-annealing duration.

The EL images (Fig. 3) for each air-annealing duration were performed under a current load equal to ~ J_{SC}. The images map the electronic quality of the absorber across the whole area of the cell. The uneven signal over the cell area can originate from the non-identical PV properties of all CIGS grains amplified by their solution-based nature and presence of local shunts and grain boundary (GB) recombination [3]. It can be seen that the signal is significantly stronger in cells annealed for over 15 min and is highest for the 30 min anneal, which is consistent with the V_{OC} values of these cells from Table I. The voltage improvement can be attributed to oxygen passivation of the surface defects such as Se vacancies. The passivation reduces surface and GB recombination [2]. After 60 min of air-annealing the signal weakened. During the anneal, the Cd diffusion from the buffer layer to the close-to-surface region is beneficial to adjust field profile in the space charge region. Further migration however damages junction stability and carrier density of the CIGS material [3]. In addition, oxygen can induce Cu migration towards the back, where it acts as a compensating donor [8].

To evaluate the doping density of the CIGS absorber, carrier density profiles displayed in Fig. 4 were extracted from the C-V measurements at room temperature. With increased annealing time, the apparent carrier density dropped by almost one order of magnitude from 2.5×10^{16} cm^{-3} (non-annealed) to 3.6×10^{15} cm^{-3} (60 min annealed). Interface states may contribute to the capacitance signal and therefore C-V measurement can give ambiguous values. Although not performed here, drive level capacitance profiling (DLCP) would be a better method of estimating the free carrier concentration due to its insensitivity to the response from interface or near-interface states [9]. Additionally, the depletion region width in Fig. 4 seems to increase with the annealing duration as the U-shape curve of the doping profile is progressively wider upon annealing. Similar observations

were reported by Rau et al after oxygenation-induced Cu$^+$ release from the surface and migration to the bulk due to the built-in electric field of the heterojunction. This in turn reduced the effective acceptor density and increased space charge region (SCR) width [8].
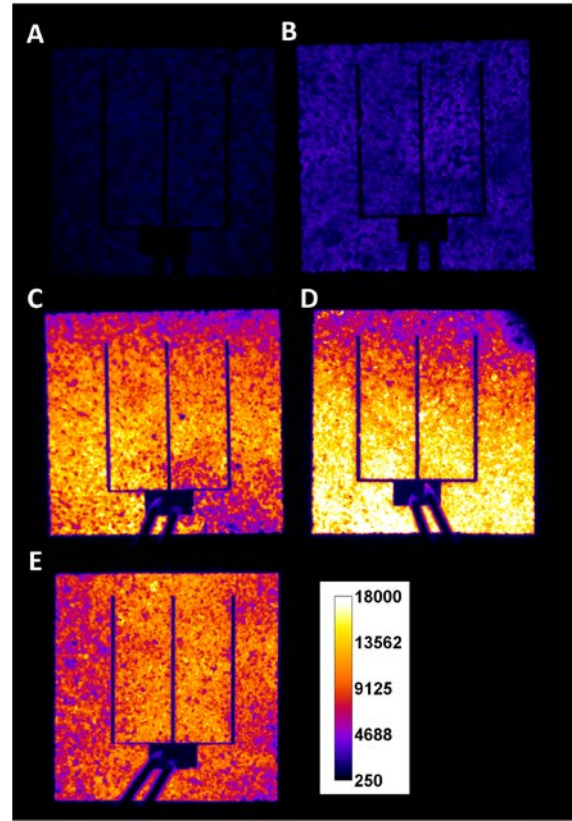

Fig. 3. EL images for a cell air-annealed for 0 min (A), 5 min (B), 15 min (C), 30 min (D) and 60 min (E).
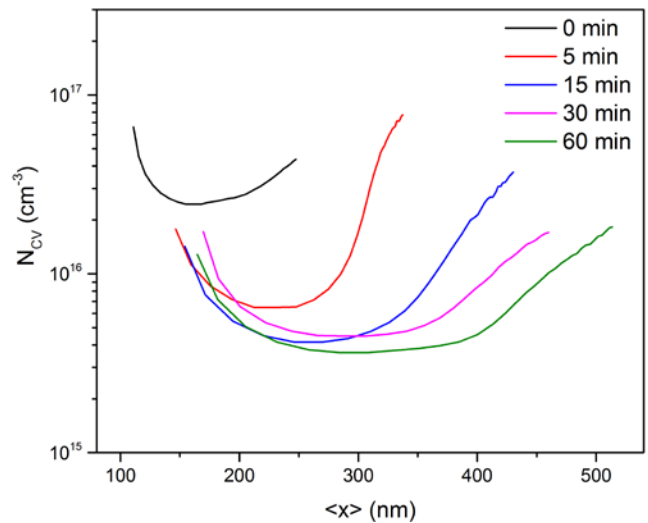

Fig. 4. Carrier density profiles extracted from C-V measurements for various air-annealing durations of CIGS/CdS.

From the EQE spectra in Fig. 5, the increase in carrier collection from 0 to 60 min annealing is observed at all wavelengths, agreeing with the gradual increase in J_{SC}. The increase in carrier collection with annealing can result from elimination of interface defects or an increased depletion width as observed in Fig. 4. All the EQE curves show a lack of long wavelength response. This can be attributed to a porous and poorly crystallized absorber near the back contact with likely weak minority carrier-collection and low carrier lifetimes deep in the absorber. Typical cross-sections of the CIGS films fabricated using the same methodology are shown in our previous work [6]. EQE spectra were used to determine the band gap (E_g) of the absorber material by fitting a plot of $[\ln(1-EQE)*E]^2$ vs. E, and are displayed in the inset of Fig. 5.
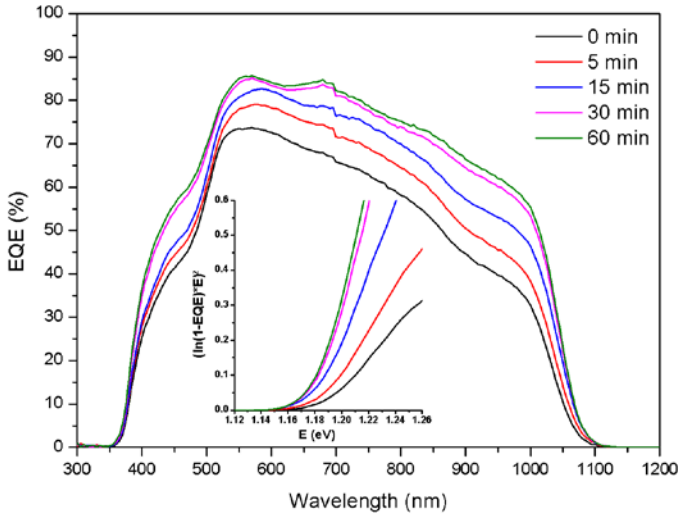

Fig. 5. EQE spectra for each annealing duration. Inset: plot of $(\ln(1-EQE)*E)^2$ vs. E, where $E=hc/\lambda$ (h is Planck's constant, c is the speed of light and λ is the wavelength of light), used to extract the band gap.

TABLE II
PV PARAMETERS OF THE BEST CELL FOR EACH ANNEALING

	E_g (eV)	E_A (eV)	E_g/q - V_{OC} (V)	N_{CV} (cm^{-3})	E_{A-AS} (meV)
0 min	1.189	1.092	0.76	24.5 x 10^{15}	70
5 min	1.185	1.240	0.73	6.49 x 10^{15}	222
15 min	1.182	1.282	0.66	4.16 x 10^{15}	244
30 min	1.182	1.278	0.62	4.49 x 10^{15}	298
60 min	1.182	1.259	0.63	3.63 x 10^{15}	273

The band gaps for all air-annealing durations are summarized in Table II along with the calculated open circuit voltage deficit (E_g/q - V_{OC}), where q is the electron charge. A slight decrease in E_g from 1.189 eV to 1.185 eV after 5 min annealing and to 1.182 eV above 15 min annealing is observed. This relatively small E_g reduction upon annealing could originate from compositional variation through the depth of the absorber due to atom migration and redistribution. No shift in the PL peak position was observed for any anneal duration however. PL spectra shown in Fig. 6 exhibited a dominant peak at 1.21 eV. All PL peaks are shifted to higher energies with respect to their band gap energy E_g (~20 meV). This shift can be caused by overheating of the sample during the measurement due to high excitation laser power applied. Moreover, due to fixed laser wavelength (640 nm) used in the measurement, the PL spectra would not show any compositional variation through the absorber depth, since the laser light would be totally absorbed in the first few hundred nanometers only. The inset of Fig. 6 shows that PL intensity was enhanced with annealing duration up to 30 min and decreased for 60 min annealing duration. The increase in PL intensity is indicative of fewer defect energy states in the absorber.
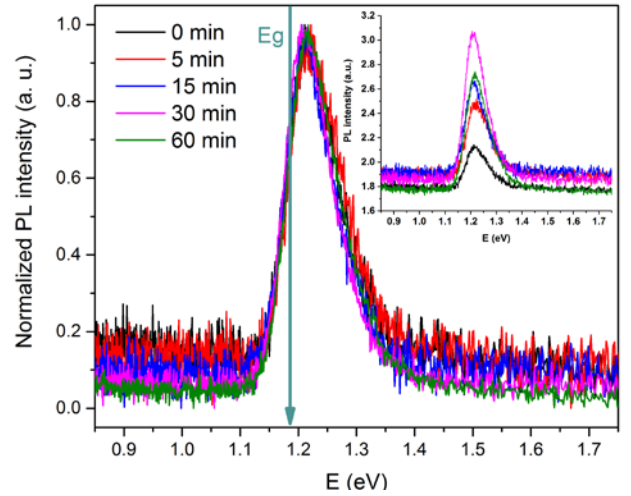

Fig. 6. Normalized PL spectra for each aannealing duration. The inset shows PL intensity of each signal.

The voltage difference between V_{OC} and Eg/q is nominally close to 0.5 V for high quality CIGS solar cells [10]. The voltage deficit is larger than 0.6 V for all the devices presented here, and this difference becomes larger with shorter annealing times. To examine the cause of the V_{OC} deficiency, temperature-dependent measurements were performed to find the dominant recombination mechanism and defect energy levels. J-V-T was performed within a temperature range of 315-105 K. The activation energy of the dominant recombination mechanism (E_A) can be extracted from the J-V-T measurements by plotting a graph of V_{OC} vs. temperature, which is presented in Fig. 7. Extrapolation of the linear part of the curves to T = 0 K gives an intercept equal to E_A/q. E_A values for each annealing duration are summarized and compared to the respective band gaps in Table II. The activation energy is equal to or close to the band gap for all annealed samples, indicating that the Shockley-Read-Hall (SRH) recombination in the bulk is the dominant recombination mechanism in the annealed samples. E_A is lower than the band gap for the non-annealed CIGS cell

however, suggesting that recombination is primarily occurring at the heterojunction interface [11]. Therefore, annealing of the CIGS/CdS is reducing recombination at this interface. Interface recombination in the non-annealed device can be a result of the presence of surface traps such as selenium vacancies, which are effectively passivated by oxygen during annealing [8].
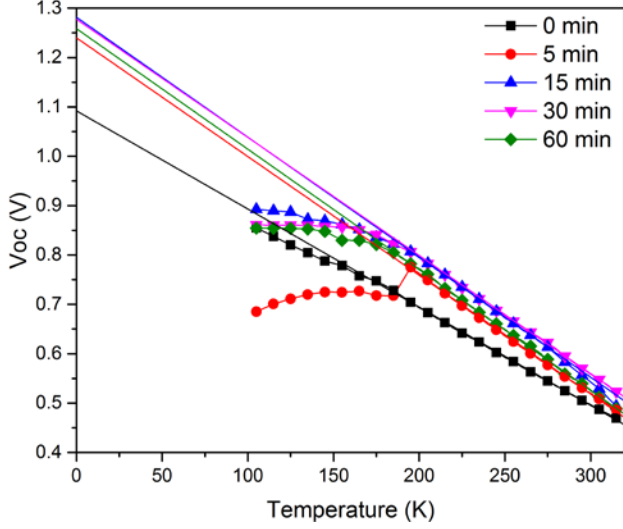

Fig. 7. V_{OC} vs. Temperature from J-V-T measurement. The intercept of the linear extrapolation at T = 0 K is equal to E_A/q.

To analyze the energetic position of the defects within the p-n junction, admittance spectroscopy was conducted in equilibrium conditions (no bias applied). This involved measuring capacitance as a function of frequency and temperature. Capacitance-frequency (C(f)) curves (Fig. 8) feature a capacitance step from low to high frequencies. At low temperatures (105 – 165 K) for the non-annealed CIGS cell, the curve features a capacitance step, which is often associated with a discrete shallow interface state N_1, with an activation energy typically in the range of 50-200 meV. There is no capacitance step observed at low temperatures for any annealed sample, however a step is present in the mid to high temperature range (165 – 315 K) for all annealed samples. A high temperature capacitance step is generally identified as a bulk acceptor defect N_2 with an activation energy of about 300 meV [12]. To calculate activation energies associated with these transitions, a curve $\ln(\omega_0/T^2)$ vs. 1000/T was plotted (Fig. 9), where $\omega_0 = 2\pi f_0$ with f_0 (transition frequency) corresponding to the inflection points of the C(f) curves. The inflection points were obtained from the peak values of the G(f) spectra, where G is the conductance. Using the Arrhenius equation, activation energies for these transitions were extracted from the slope of the curves in Fig. 9 and are summarized in Table II under the abbreviation E_{A-AS}. An admittance response with activation energy of about 70 meV was obtained in the non-annealed sample, close to the energy level of V_{Cu} defect. Shifts in the positions of N_1 and N_2 defects

as compared to the literature might be due to the particular precursor solution chemistry or selenization process [12]. In all annealed devices, shallow defects at low temperatures possibly attributed to V_{Se} or V_{Cu} are not present. The shallow interface state observed in the non-annealed sample seemed to sink into deeper energy levels with annealing however. It was observed at energy levels of 222, 244, 298 and 273 meV for annealing times of 5, 15, 30 and 60 min respectively. Rau *et al* suggests that Se vacancies might be passivated by O atoms. Additionally, Cd ions from the chemical bath might occupy Cu sites close to the surface, partially restoring the positive surface charge. Finally, Cu is a fast diffuser and its migration deeper in the bulk is driven by the electric field caused by the heterojunction [8].
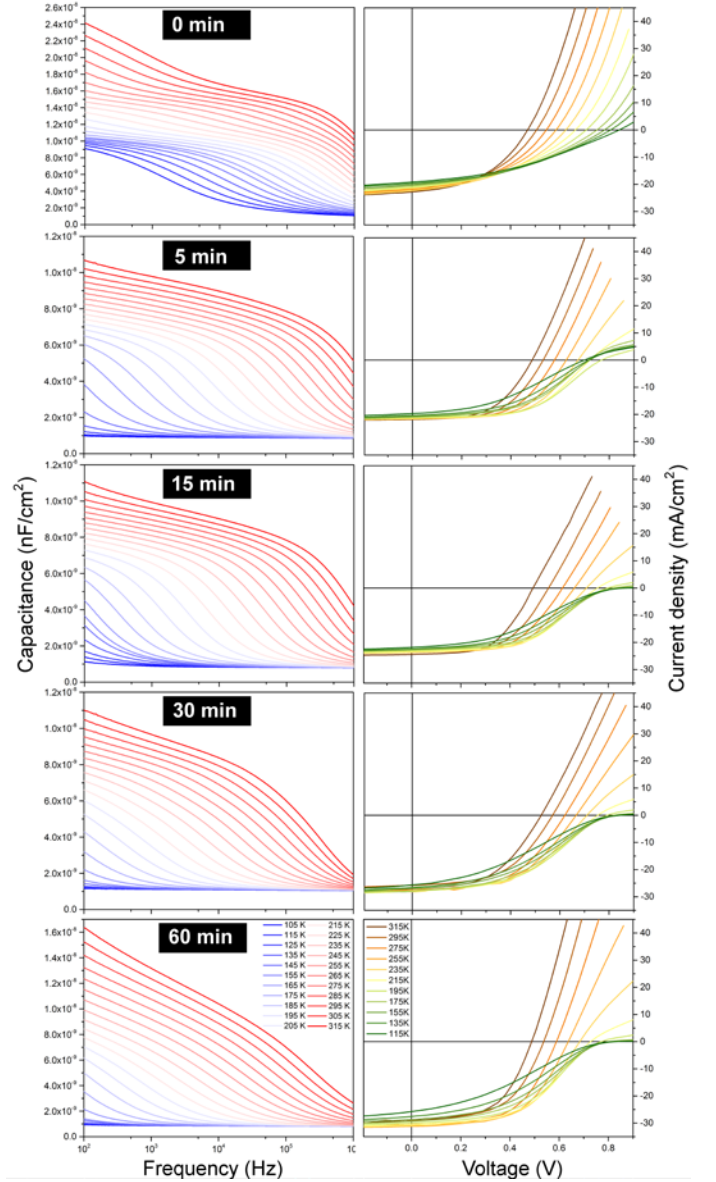

Fig. 8. Admittance spectra in the dark at 0 V bias (left) and J-V-T curves (right) of CIGS/CdS annealed for various durations.
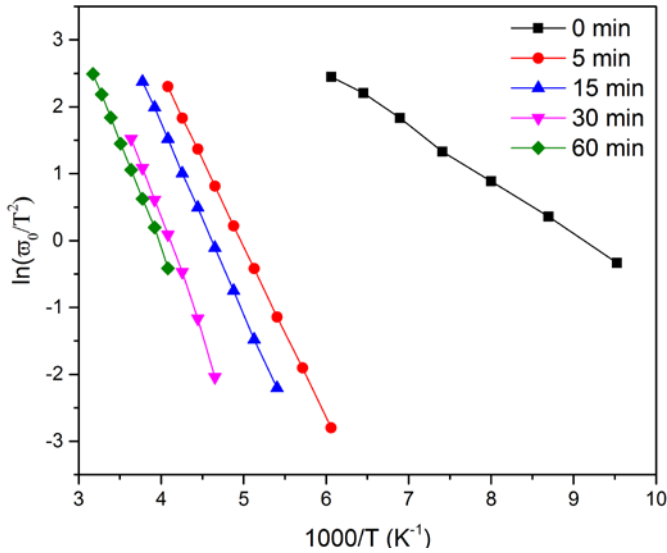
Fig. 9.   The Arrhenius plot of the admittance spectroscopy data.

J-V-T curves displayed in Fig. 8 reveal that efficiencies collapse towards lower temperatures, primarily due to the collapse of the fill factor. This can in turn be related to a dramatic increase in series resistance that quenches the fill factor. Another feature observed from the J-V-T curves is the presence of rollover at low temperatures, which appears in all annealed samples. The rollover and crossover between light and dark J-V can be indicative of the presence of a blocking back contact at the Mo/CIGS interface [12], which perhaps becomes more severe with longer annealing times.

IV. CONCLUSIONS

The effect of air-annealing on the electrical properties of solution-processed CIGS/CdS films was studied. The annealed devices exhibited an increase in all PV indicators up to 30 min of annealing. Further annealing was no longer beneficial to the device performance; on the contrary a wider space charge region could lead to enhanced recombination. Scattered performances can be caused by the uneven heat distribution in the furnace used for annealing. It was concluded that the interface states such as Se vacancies were effectively passivated by oxygen atoms removing shallow interfacial defects located at the CIGS/CdS heterointerface. Mobile Cu ions diffuse deep into the absorber however, reducing the effective doping density. The electrical behavior of the CIGS solar cells is heavily influenced by deep level defects in the bulk of the space charge region and at the heterojunction interface. The admittance spectra, capacitance profiling and phenomena such as rollover seen in the presented air-annealed CIGS solar cells are very difficult to interpret and are very sensitive to specific assumptions about material properties. Understanding the electrical characterization is nonetheless a necessary step for further improvement of these amine/thiol-based solution-processed CIGS solar cells.

REFERENCES

[1] T. K. Todorov, O. Gunawan, T. Gokmen, and D. B. Mitzi, "Solution-processed $Cu(In,Ga)(S,Se)_2$ absorber yielding a 15.2% efficient solar cell," *Prog. Photovoltaics Res. Appl.*, vol. 21, no. 1, pp. 82–87, 2013.

[2] P. Arnou, C. S. Cooper, S. Uličná, A. Abbas, A. Eeles, L. D. Wright, A. V. Malkov, J. M. Walls, and J. W. Bowers, "Solution processing of $CuIn(S,Se)_2$ and $Cu(In,Ga)(S,Se)_2$ thin film solar cells using metal chalcogenide precursors," *Thin Solid Films*, vol. 633, pp. 76–80, 2016.

[3] Y. M. Shin, C. S. Lee, D. H. Shin, H. S. Kwon, B. G. Park, and B. T. Ahn, "Surface modification of CIGS film by annealing and its effect on the band structure and photovoltaic properties of CIGS solar cells," *Curr. Appl. Phys.*, vol. 15, no. 1, pp. 18-24, 2015.

[4] U. Rau and M. Schmidt, "Electronic properties of $ZnO/CdS/Cu(In,Ga)Se_2$ solar cells - Aspects of heterojunction formation," *Thin Solid Films*, vol. 387, no. 1–2, pp. 141–146, 2001.

[5] T. Eisenbarth, T. Unold, R. Caballero, C. A. Kaufmann, and H. W. Schock, "Interpretation of admittance, capacitance-voltage, and current-voltage signatures in $Cu(In,Ga)Se_2$ thin film solar cells," *J. Appl. Phys.*, vol. 107, no. 3, 2010.

[6] S. Uličná, P. Arnou, A. Eeles, M. Togay, L. D. Wright, A. Abbas, V. Malkov, J. M. Walls, and J. W. Bowers, "Control of $MoSe_2$ formation in hydrazine-free solution-processed CIS/CIGS thin film solar cells." 44th *IEEE Photovoltaic Specialist Conference*, 2017.

[7] C. W. Jeon, T. Cheon, H. Kim, M. S. Kwon, and S. H. Kim, "Controlled formation of $MoSe_2$ by MoNx thin film as a diffusion barrier against Se during selenization annealing for CIGS solar cell," *J. Alloys Compd.*, vol. 644, pp. 317–323, 2015.

[8] U. Rau, D. Braunger, R. Herberholz, H. W. Schock, J.-F. Guillemoles, L. Kronik, and D. Cahen, "Oxygenation and air-annealing effects on the electronic properties of $Cu(In,Ga)Se_2$ films and devices," *J. Appl. Phys.*, vol. 86, no. 1, pp. 497–505, 1999.

[9] L. Yin, G. Cheng, Y. Feng, Z. Li, C. Yang, and X. Xiao, "Limitation factors for the performance of kesterite $Cu_2 ZnSnS_4$ thin film solar cells studied by defect characterization," *RSC Adv.*, vol. 5, no. 50, pp. 40369–40374, 2015.

[10] V. Nadenau, U. Rau, A. Jasenek, and H. W. Schock, "Electronic properties of $CuGaSe_2$-based heterojunction solar cells. Part I. Transport analysis," *J. Appl. Phys.*, vol. 87, no. 1, pp. 584–593, 2000.

[11] O. Gunawan, T. K. Todorov, and D. B. Mitzi, "Loss mechanisms in hydrazine-processed $Cu_2ZnSn(Se,S)_4$ solar cells," *Appl. Phys. Lett.*, vol. 97, no. 23, p. 233506, 2010.

[12] T. Kobayashi, Z. J. L. Kao, and T. Nakada, "Temperature dependent current-voltage and admittance spectroscopy on heat-light soaking effects of $Cu(In,Ga)Se_2$ solar cells with ALD-Zn(O,S) and CBD-ZnS(O,OH) buffer layers," *Sol. Energy Mater. Sol. Cells*, vol. 143, pp. 159–167, 2015.